

**Idiopathic pulmonary fibrosis: A mechanistic study
using morphologic and functional data in a
computational lung model**

Yuwen Zhang

A thesis submitted in fulfilment of the requirements for the degree of Doctor of
Philosophy in Bioengineering.

This thesis is for examination purposes only and is confidential to the examination
process.

Auckland Bioengineering Institute

The University of Auckland

2018

Abstract

The content of abstract

Acknowledgement

I would like to thank...

Table of Contents

| | |
|---|------|
| Abstract | iii |
| Acknowledgement | v |
| Table of Contents | ix |
| List of Figures | xiii |
| List of Tables | xv |
| List of Abbreviations | xv |
| 1 Introduction | 1 |
| 1.1 Motivation | 1 |
| 1.2 Aim | 2 |
| 1.3 Thesis Overview | 2 |
| 2 Pulmonary lobar segmentation from CT scans | 3 |
| 2.1 Aim of pulmonary lobar segmentation | 3 |
| 2.2 challenges of pulmonary lobar segmentation | 5 |
| 2.3 review of current published methods of pulmonary lobar segmentation . | 6 |

| | | |
|----------|---|-----------|
| 2.3.1 | Lung segmentation | 6 |
| 2.3.2 | Fissure detection | 11 |
| 2.4 | Automatic statistical shape model based lobar segmentation method . . | 15 |
| 2.4.1 | Lung segmentation | 15 |
| 2.4.2 | Statistical finite element models of lung and fissure shape | 15 |
| 2.4.3 | Initial prediction of lobar location in an individual | 17 |
| 2.4.4 | Multiscale Hessian-based fissure detection | 18 |
| 2.4.5 | Interactive user control interface | 21 |
| 2.5 | Experiment | 23 |
| 2.5.1 | Data | 23 |
| 2.5.2 | Result | 24 |
| 2.6 | Discussion | 26 |
| 3 | Quantitative analysis of idiopathic pulmonary fibrosis abnormality from CT scans | 29 |
| 3.1 | Challenges of IPF diagnosis | 29 |
| 3.2 | Advantages of quantitative analysis using HRCT | 30 |
| 3.3 | Review of current published methods of quantitative analysis of IPF . . | 31 |
| 3.4 | Method of IPF quantitative analysis | 32 |
| 3.4.1 | Pulmonary parenchymal classification | 32 |
| 3.4.2 | Normalization of classified data | 34 |
| 3.4.3 | Quantitative analysis of imaging data | 36 |
| 3.5 | Experiment | 39 |
| 3.5.1 | Imaging and clinical data | 39 |
| 3.5.2 | Results | 39 |

| | |
|---|-----------|
| 3.6 Discussion | 48 |
| 4 Functional model based analysis of IPF | 53 |
| 4.1 Functional model introduction | 53 |
| 4.2 Section 2 | 53 |
| 5 Conclusion | 55 |
| 5.1 Summary | 55 |
| 5.2 Limitations | 55 |
| 5.3 Future directions | 55 |
| List of References | 57 |

List of Figures

| | | |
|-----|--|----|
| 2.1 | SSM initial fissure prediction results. (a) Lung surface fitting and manually-digitized fissure data. (b) Procrustes aligned meshes of 30 subjects. (c) (d) Fissure prediction (white) compared to ground truth fissure points. . . | 19 |
| 2.2 | Hessian-based multiscale fissure detection results. (a) Hessian-based fissure enhancement. (b) Remove vessel voxels. (c) ROI of fissure locations based on SSM projection. (d) 2D and 3D eigenvector based connected component filter. (e) Fissure candidate points. (f) B-spline curve fissure surface fitting. | 22 |
| 2.3 | User interactive interface. | 23 |
| 2.4 | Quantitative evaluation results of the segmentation accuracy. (a) Mean difference for normal young subjects. (b) Mean difference for IPF subjects. | 25 |
| 2.5 | The spatial distribution of error between the gold-standard and semi-automatic methods for three representative subjects, highlighting localized regions of low accuracy. | 26 |

| | | |
|-----|--|----|
| 3.1 | Color labelled classification result of case 7 on IPF HRCT by CALIPER. (a) Transverse plane. (b) Coronal plane. (c) Sagittal plane. (d) 3D color labelled lung. | 33 |
| 3.2 | Classified data normalization result of three time points for case 6. (a) SSM based mapping result of the three time points. (b) Ununiformed gap slice after mapping. (c) Gap filled slice of the three time points. The three time points are shown in the same position and same slice number. | 36 |
| 3.3 | Subpleural-to-internal percentage calculation diagram. | 38 |
| 3.4 | Average density (g/cm ³) of each CT pattern for IPF left and right lung. Each point represents the average density of one CT pattern for each lung. X axis shows the month interval of scan time for each patient, and 0 represents the first scan for this patient. (a) Left lung. (b) Right lung. | 40 |
| 3.5 | Volume percentage change of each CT pattern over time for case 6. (a) Left lung. (b) Right lung.. | 41 |
| 3.6 | Percentage of each disease CT pattern against lung height (dorsoventral axis) for IPF left and right lung. The region percentage was calculated averagely within 5% of the lung height from the base to the apex. Red line represents the average value of this position across all patient, and blue line shows the standard deviation. (a) (b) is the ground-glass pat- tern distribution against lung height for left and right lung. (c) (d) is the reticular pattern distribution against lung height for left and right lung. (e) (f) is the honeycomb pattern distribution against lung height for left and right lung. (g) (h) is the emphysema pattern distribution against lung height for left and right lung. | 43 |

| | |
|---|----|
| 3.7 Lobar distribution of CT patterns. X axis shows the month interval of scan time for each patient, and 0 represents the first scan for this patient. Each point represents the percentage of one CT pattern for one lobe. The dotted line represents the average value for each time point. (a) Ground-glass lobar distribution. (b) Reticular lobar distribution. (c) Honeycomb lobar distribution. (d) Emphysema lobar distribution. | 44 |
| 3.8 Subpleural-to-internal percentage of connected CT pattern cluster for IPF left and right lung. (a) Left lung. (b) Right lung. | 45 |
| 3.9 Shape differences between IPF subjects and normal subjects for the first three mode (a) Mode 1. (b) Mode 2. (c) Mode 3. Arrow tracks the mode weight changes over time. | 48 |
| 3.10 Mahalonobis distance of IPF subjects | 49 |

List of Tables

| | | |
|-----|--|----|
| 3.1 | Demographic data. | 39 |
| 3.2 | Whole volume of left and right for each time point($1.0e_5 * mm_3$). | 42 |
| 3.3 | CT pattern change over time of left lung for case 6 (%). | 46 |
| 3.4 | CT pattern change over time of left lung for case 6 (%). | 47 |

Chapter 1

Introduction

1.1 Motivation

Idiopathic pulmonary fibrosis (IPF) is a lethal fibrosing lung disorder that typically occurs in the sixth to seventh decade. IPF is more frequent in males than females, and is associated with a smoking or dust exposure. There is no known cure. Some very new therapies have been suggested to slow the rate of physiologic decline. The aetiology of IPF remains elusive with genetics (telomerase mutations and MUC5B polymorphisms), exposures and ageing all thought to contribute. More recently, lung epithelial stress associated with mechanical stretch during inflation has been proposed to explain the characteristic peripheral and basal distribution of the fibrotic insult (Selman and Pardo, 2014). Stretch overload with resultant damage to the epithelium and basement membrane scaffolding may disrupt spatial orientation of epithelial airway cells during healing and result in an aberrant fibrotic response to injury such as infection, microaspiration or smoke inhalation. There has been some limited modelling of the impact of the impact of stretch on the peripheral lung in IPF (Carloni et al., 2013), however we are not aware

of any data arising from computational methods that integrate image and physiologic data.

1.2 Aim

1.3 Thesis Overview

Chapter 2 Pulmonary lobe segmentation.

Chapter 3 Quantitative analysis of IPF.

Chapter 4 Functional model based analysis of IPF.

Chapter 5 Conclusion.

Chapter 2

Pulmonary lobar segmentation from CT scans

The following chapter outline the study of pulmonary lobar segmentation using CT scans based on a statistical shape model, which is an important step before the future lobar based analysis. This chapter is divided into (1) aim of pulmonary lobar segmentation, (2) challenges of pulmonary lobar segmentation, (3) review of current published methods of pulmonary lobar segmentation, (4) automatic statistical shape model based lobar segmentation method, (5) interactive user control interface developed on pulmonary toolkit, (6) experiment and (7) discussion.

2.1 Aim of pulmonary lobar segmentation

Pulmonary lobe anatomy

Human lungs are divided into five distinct anatomical regions, which are called the pulmonary lobes. These lobes separate airways and vessel trees into different branches,

and are largely anatomical independent. The separating junctions between these lobes are called the lobar fissures. The left lung consists of the left upper lobe and left lower lobe, which are separated by the left oblique fissure (major fissure). The right lung consists of the right upper lobe, right middle lobe and right lower lobe, which are separated by right oblique fissure (major fissure) and right horizontal fissure (minor fissure) (See Figure 1). These fissures contain pleural fluid and provide separation between the lobes while permitting some relative movement. In general, the functions of these lobes are relatively independent with each other since there are no major airways and vessels crossing the lobar fissures (Lassen et al 2010).

The importance of pulmonary lobar segmentation

The extraction of these lobes is of great importance in applications of lung disease assessment and treatment planning. For clinical applications, the distribution and location of pulmonary disease are beneficial for doctors to recognize pathogenesis, guide therapy and have further value in surgical planning. That is because many pulmonary diseases are more prevalent in specific anatomic regions of the lung, which means that many lung diseases act as a lobar level. For example, emphysema (Jeffery et al 1998), postprimary tuberculosis (Leung et al 1999) and silicosis (Rees et al 2007) usually affect the upper lobes, while idiopathic pulmonary fibrosis is commonly present in the lower lobes. However, there is currently a lack of quantitative and objective methods for the regional assessment of lung disease. Therefore, techniques are really necessary for identifying the location, shape and volume of the lobes so that lung disease could be measured at a lobar level and the severity could be assessed accurately.

2.2 challenges of pulmonary lobar segmentation

Currently, the most traditional method for CT scans lobe segmentation is tracking the lobar boundaries manually by an experienced pulmonary radiologist. However, the process of determining the lobar boundaries is an extremely laborious and time-consuming task, since a 3D high-resolution CT imaging subject may contain a large number of axial sections which makes the manual segmentation very time consuming, typically taking hours for one patient. Therefore, rare doctors use manual lobe segmentation in clinical diagnosis and treatment practice and most clinicians think visual observation subjectively is more effective and convenient. For this reason, an automatic (no user interaction) or semi-automatic (minimal user interaction) lobe segmentation techniques is urgently needed in clinical applications and it has attracted great interest of researchers all over the world. However, to find an effective and time-saving automatic lobe segmentation method is a challenging task because of anatomical variation and incomplete fissures. On one hand, lobes vary between subjects. The anatomical variation of lobe is usually associated with age, sex and body type. Pathologies of diseased lungs usually deform the lobar shape abnormally and result in some fuzzy appearance of fissures on CT images, in particular in the presence of abnormalities near the fissures, which makes fissure segmentation challenging. On the other hand, even in patients with healthy lung parenchyma the fissures are usually incomplete (Glsn et al 2006) (see Figure 2).

2.3 review of current published methods of pulmonary lobar segmentation

In a broad sense, the existing computational lobe segmentation methods usually consist of two steps: the segmentation of lungs and the detection of the three main pulmonary fissures which divide the lungs into five lobes. Currently, quite a number of lung segmentation methods are well established to get a reliable result. In contrast, most challenges for automated lobar segmentation lie in the fissure detection. Fissure detection is a hot research field and quite a lot of algorithms has been developed both in 2D and 3D, however, no method has yet been demonstrated to be robust and effective across a wide range of subject especially abnormal subject. To some extent, lung segmentation and fissure detection are two independent parts and can be improved separately. That means it would be possible for us to change lung segmentation to another one without affecting the fissure detecting result dramatically.

2.3.1 Lung segmentation

The segmentation of lung is the prerequisite for the accomplishment of lobe segmentation, as it can provide a boundary condition for the subsequent fissure detection, specify the position when extending the fissure surface and allow the estimation of lung volumes and the detection and quantification of abnormalities within the lungs. So far, a large number of researches have been involved in the hot topic of lung segmentation from CT scans and most of the published methods can perform well. In CT scans from healthy subjects, the air-filled lung parenchyma usually has a different attenuation compared to surrounding tissue. For this reason, quite a lot of conventional lung

segmentation algorithms are based on a thresholding approach. Threshold value is acquired from gray level histogram analysis and then the largest connected component region is detected or region growing method working on airways is used to find the lung region initially. Some thresholding algorithms, especially the ones in old papers, are developed in 2D space, which means each axial section of CT imaging need to be calculated separately (e.g. Kalender et al 1991, Kemerink et al 1998, Leader et al 2003, Armato and Sensakovic 2004). But this process may cause incontinuity between slices, hence a further improved 3D processing (Hu et al 2001, Ukil and Reinhardt 2005, Sun et al 2006) is a better choice and has been widely used in a lot of papers. 3D thresholding algorithms avoid inconsistencies between slices and is less time consuming as well. Although gray-level thresholding information was considered to help with finding the lung boundaries and studying on lung structures from early times (Keller et al 1981, Hedlund et al 1982, Hoffman et al 1983, 1985(a), 1985(b)), these methods usually combined with much manual interaction, such as manually selecting threshold values or seed point for region growing and separating left and right lung manually. That means the whole process may be too time consuming and cause too many personal errors. Hu et al (2001) was the first research group to apply threshold-based algorithm in a fully automatic lung segmentation method. In their study, the lung region was firstly extracted from the CT images by gray-level thresholding processing. The left and right lungs were then separated by identifying the anterior and posterior junctions by dynamic programming. Finally, a sequence of morphological operations was used to smooth the irregular boundary along the mediastinum in order to obtain results consistent with those obtained by manual analysis, in which only the most central pulmonary arteries were excluded from the lung region. Considering the problem of inconsistent boundaries caused by irregular and inconsistent lung boundary for the regions near the

mediastinum, Ukil and Reinhardt (2005) developed a further improved automatic lung segmentation method for the three-dimensional smoothing of the lung boundary using information from the segmented human airway trees. First, a bounding box was defined around the mediastinum for each lung using the information from the segmented human airway trees, and all operations were performed within the bounding box. Then, all generations of the airway tree distal were defined to the right and left main stem bronchi to be part of the respective lungs and all the other segmented structures could be excluded. Finally, a fast morphological closing with an ellipsoidal kernel was performed to smooth the surface of the lung. Sun et al (2006) also presented a 3D-based method for segmenting and visualizing lung volume using CT images. The improved point of this paper is that an anisotropic filtering method was firstly applied on CT slices to enhance the signal-to-noise ratio. A wavelet transform-based interpolation method was subsequently used followed to construct the 3D volumetric CT slice data with volume rendering. After that, an adaptive 3D region-growing algorithm was developed to detect lung region, combined with automatic seed-locating methods. Fuzzy logic algorithms and 3D morphological closing approaches were finally used to refine the lung volume and fill the holes in it. The segmentation method was tested on 20 CT scans and the results showed the segmentation method was effective and robust with an average accuracy rate of 88.5As we mentioned above, though conventional threshold-based methods are fast, robust and accurate for healthy subjects, they may fail to perform well scans containing pathologic abnormalities, and such an approach often results in segmentation errors and requires clinicians to manually edit the results. Currently, the published specially designed lung segmentation methods (e.g. Kitasaka et al 2003, Sluimer et al, 2005, Pu et al, 2008, 2011, Prasad et al 2008, Korfiatis et al 2008, Wang et al, 2009, van Rikxoort et al 2009, Sun et al 2012) mostly aim at one kind of disease and therefore could not

get a good result across a large population. To deal with the problem of lesions adjacent to the chest wall and mediastinum, Kitasaka (2003) developed a lung area extraction method using a shape model. A contour shape model using a Bzier surface was fitted to the contour surface of the individual input images with an affine transformation method. Then, an active contour model was utilized to refine the initial segmentation. The results showed that by using the proposed technique to 3D chest X-ray CT images, most lesions could be identified accurately. However, because the lung apex and base were not included in the model, lesions adjacent to the lung apex or diaphragm could result in segmentation errors. Pu et al (2008) presented a lung segmentation algorithm based on adaptive border marching (ABM) to include juxtapleural nodules in the lung region since these juxtapleural may be excluded from the results calculated by a conventional threshold-based algorithm. The adaptive border marching algorithm could smooth the lung borders after a initial thresholding processing and minimize oversegmentation of adjacent regions such as the abdomen and mediastinum at well. The method was tested on 20 datasets and the results demonstrated that this method could re-included all juxtapleural nodules in the lung regions. An average oversegmentation ratio of this method was 0.43 % which was lower than the reference standard average segmentation determined by an expert. The whole calculation process could be completed in a very short time with under 1 min for one subject on a typical PC. In order to deal with the problem of various diseases, image noise or artifacts and individual anatomical variety, Pu et al (2011) developed a shape analysis strategy termed break-and-repair. A principle curvature analysis was applied to eliminate the problematic regions and then radial basis function (RBF) based implicit surface fitting was used to get a smooth lung surface. To overcome the problem of error detection for lung pathologies, Prasad et al (2008) made use of the rib curvature information to help with finding the lung borders. The method

was based on a threshold-based algorithm followed by morphologic operation and the core principle of the method was adapt the threshold value to individual subject by making the curvature of lung along the ribs be similar to the curvature of the ribs. The curve of the ribs and lung boundary were both represented by polynomial interpolation even though there was minimal deviation from this representation. The method was evaluated by comparing to conventional lung segmentation techniques on 25 subjects using a volumetric overlap fraction measure and the results showed that the performance of the rib segmentation method was quite different from the conventional one. Wang et al (2009) proposed a texture analysis-based method for accurate segmentation of lungs with CT scans. The lung region including normal and mild ILD lung parenchyma was first segmented by a CT value thresholding technique and then texture-feature images derived from the co-occurrence matrix was used to identify abnormal lung regions with severe ILD from the initial results. 2D holes filling was applied to smooth the final lung segmentation. The overlap rate, volume agreement, mean absolute distance (MAD), and maximum absolute distance between the automatically segmented lungs and the reference lungs delineated by a medical physicist manually were employed to evaluate the performance of the segmentation method. On the basis of the previous studies, Sun et al (2012) developed a further approach for segmentation of lungs with high-density pathologies. The method had two main steps. In the first step, a robust active shape model (RASM) matching method was utilized to roughly find the outline of the lungs. To initialize the shape model of RASM, the detected rib information was used subsequently. In the second step, an optimal surface finding approach was applied to further adapt the initial segmentation result to the lung. The method was evaluated on 30 data sets with 40 abnormal (lung cancer) and 20 normal left/right lungs with a result of an average dice coefficient of 0.975 ± 0.0006 and a mean absolute surface distance error

of 0.84 ± 0.23 mm.

2.3.2 Fissure detection

Fissures are the most visible boundaries between the lobes, and therefore the detection of fissure points is an essential part of any accurate lobe segmentation method. The currently published fissure detection method can be mainly classified into two categories. The first category is named anatomy knowledge based method. This kind of method usually depends on either local or global knowledge of the anatomy of lung structure based on two features of lungs. The first feature is the fact that there should not be any large vessels in the vicinity of lobar fissures, so fissures should be located in the gaps between airway and vessel trees. Another feature is the vessels and bronchi could be classified into five lobe regions using an edge detection method. A number of published papers use the segmentation results of airways and vasculature to help with localizing the fissures. Kuhnigk et al (2003 2005) was early group to present a framework of making use of lobar airways and vasculature into account for automatic fissure detection. A watershed transformation method was used to take an analysis of these anatomical structures and this method was widely used and improved by other researches later, but the results with the simple algorithm was still inaccurate even for some clearly visible fissures. Ukil and Reinhardt (2009) developed Khnigks fissure detection method which combined a distance transform to segmented vessels and original chest CT scan as a cost image for a watershed transform guided by airway and vascular markers. The improved watershed transform algorithm could provide a close initial approximation to the lobar fissures and an initial search area for the lobar fissures was determined. Subsequently, a further refinement method was used to construct a region of interest (ROI) encompass-

ing the fissures and a 3D optimal surface detection algorithm combined with a ridgeness measure based on the structure tensor analysis was then applied to enhance the ROI and finally find the optimal surface within the ROI. In the last step, incomplete fissures were smoothly extrapolated using a fast-marching method based segmentation of a projection of the optimal surface. The method was evaluated by comparing the automatic results to manual tracings of the fissures with 12 normal subjects and 17 diseased subjects. The RMS errors for the left oblique fissure, right oblique fissure and right horizontal fissure were 1.81, 1.57, 1.43mm respectively of the normal subjects and 1.71, 1.88, 2.31 respectively of the abnormal subjects. However, some manual operations were still needed for about 20%-25% subjects.], Lassen et al (2011) also described the fissure detection method by building a cost image for the watershed transformed segmentation which is an extension of the framework of Kuhnigk. The interactive segmentation method was tested on 25 CT scans comparing to a manual segmentation by a human observer and showed an average distance of 1.57+- 0.3mm. In addition, Zhou et al (2004) and Saita et al (2006) took advantage of the linear appearance of fissures to class the vessels and bronchi into five lobe regions using an edge detection method and the Hough transform based curved surface detection method, respectively. The second category of fissure detection is named shape based analysis method. This kind of method commonly makes use of gray-level information and shape information to detect the fissures. Generally, lobar fissures can be regarded as bright planes crossing the pulmonary volume because of the higher density value of fissures comparing to the surrounding tissues. Based on this information, quite a number of published methods use local filtering algorithm to detect the voxels which lie on these planes, so that these detected voxel points can construct a continuous fissure surface. In 2D space, the fissure appears as a clear curve, therefore some early papers usually detected fissure points based on gray-level infor-

mation in 2D space (Wang et al 2003, 2006, Kuhnigk et al 2003). For example, Wang et al (2003 2006) presented an approach for segmenting the major fissures on CT scans based on shape information. The fissure was initially denoted as a curve based on the prior knowledge of the shape of the fissure to identify the surrounding region of fissure, called fissure region for subsequent automatic segmentation. Next an image transformation called ridge map was proposed for enhancing the appearance of initial fissures. The shape-based curve-growing growing method modeled by a Bayesian network could then be applied to this map to segment the fissure. The method was applied to segment the fissures of chest CT of 10 patients with pulmonary nodules. The result showed that only 2.4% of the fissures required manual correction and the average distance between the automatic and manual segmented fissures was 1.01 mm. In 3D space, the most common used method to detect these pulmonary fissure plane structures is taking an eigenvalue analysis of Hessian matrix (Frangi et al 1998, Wiemker et al 2005(a), Kitasaka et al 2006, Ochs et al 2007, van Rikxoot et al 2008, Ukil and Reinhardt 2009, Lassen et al 2011 2013, Ross et al 2010, Doel et al 2012). Frangi et al (1998) was the first to present eigenvalue analysis of Hessian matrix to detect plane structure such as fissure and tube structure such as vessel on CT images. The three eigenvalues of Hessian matrix gives a fissure probability for each voxel and the relation between the eigenvalues of the Hessian matrix describes the local image structure (Wiemker et al 2005(b)). Wiemker et al (2005(b)) was also an early paper to use Hessian matrix for fissure detection and two 3D filter approaches were proposed in this paper. The first filter was based on first derivatives of the image gray values and utilized the eigenvalues of the local structure tensor. The second filter was based on second derivatives and utilized the eigenvalues of the local Hessian matrix. Ochs et al (2007), van Rikxoot et al (2008) both used a pattern recognition approach to detect pulmonary fissures com-

bined with eigenvalue analysis of Hessian matrix as feature and classification was also performed on these fissures. Lassen et al (2011 2013) utilized the eigenvalue analysis of Hessian matrix based on the initial approximation fissures from anatomical structure of airway and vessel trees. This algorithm combined with two types of methods could reduce many false points since the first anatomic-based method could find a region of interest which made the analysis of Hessian matrix only work in the surrounding area of the initial guessing fissure locations. Subsequently, morphological operations such as direction-based connected component analysis were also used to further reduce some non-fissure points. The average distance between automatic fissures and the reference for 55 CT scans were 0.98 mm, 3.97 mm and 3.09 mm for the left oblique fissure, right oblique fissure and right horizontal fissure respectively. Ross et al (2010) proposed a particle system that sampled the image domain combined with Hessian matrix to get a set of candidate fissure locations. A maximum a posteriori (MAP) estimation was followed to eliminate false candidate points and a post-processing operation was applied to remove remaining noise points. A thin plate spline (TPS) interpolating surface fitting method was lasted performed to form the finial fissure surfaces. Doel et al (2012) also made use of both anatomy knowledge based method and Hessian matrix to find a set of fissure candidates and proposed a smooth multi-level B-spline curve through the fissure points and extrapolated to the lung borders to get the fissure surfaces.

2.4 Automatic statistical shape model based lobar segmentation method

A three-step approach is followed for the lobe segmentation (Fig 1): in the first step, a threshold-based lung segmentation method defines the lung boundary; in the second step, a statistical shape model (SSM) is deformed to provide a search region for fissure locations; in the third step, fissures are located using a Hessian matrix protocol combined with connected component filters and a surface fitting algorithm.

2.4.1 Lung segmentation

A commonly used thresholding method is used to segment the lungs [5]. The method uses a thresholding operation (-775 Hounsfield Units) and connected component identification to find an initial approximation to the lung regions and trachea location. Using the most apical point of the trachea as a start point, a region growing technique is applied to detect the airway trees. Then, left and right lungs are separated as the two largest connected components remaining after removing the trachea and the left and right main bronchi.

2.4.2 Statistical finite element models of lung and fissure shape

To guide fissure detection, a statistical shape model (SSM) based on an active shape model (ASM) [10] of the lung was derived from a training set of segmented lung and fissure surface locations. The training set consisted of data from 30 healthy non-smokers (15 males and 15 females) that was retrospectively selected from the Human Lung Atlas (HLA) database (image acquisition for this previous study was approved by the local

ethics and radiation safety committees, and subjects gave informed consent). Lung surface segmentation was conducted as described in section 2.1; fissure surface segmentation was performed manually using the open-source visualization software CMGUI (<https://www.cmiss.org/cogui>) by an expert user, to provide a gold-standard definition of the fissure location for each subject in the training set. A finite element surface mesh was used to describe the shape of the lung and its fissures in terms of the ASM (and, in section 2.3, to define initial fissure location in the segmentation algorithm). A high order (bi-cubic Hermite) finite element mesh template with the same mesh connectivity for each subject was geometry fitted to the lung and fissure surface data for each subject. The template mesh for the left lung mesh has 35 nodes and 44 elements, while the right lung mesh has 50 nodes and 62 elements. Each node has 12 degrees of freedom (DoF) which store the global coordinates and first and second nodal derivatives. Each node is either an anatomical landmark (the left/right lung apex, the base vertex, the shape corner and the center point of the middle line of fissure) or a pseudo-landmark (e.g. a specific proportion of the arc-length between two anatomical landmarks). A least squares fit of the mesh to the lung and fissure surface data was conducted using CMISS (<https://www.cmiss.org>), which is a finite element modeling environment. The average root mean square (RMS) error of this fitting method was 0.52 mm for the 30 training subjects (Fig 2(a)). To construct the SSM, the location and derivatives at each node (landmark or pseudo-landmark) in the finite element mesh was used in a principal component analysis (PCA) conducted on the training set. To remove orientation and scaling differences between shapes, a general procrustes alignment (GPA) method was used to minimize the distance between subject meshes through calculating an optimal rotation matrix and translation (Fig 2(b)) [11]. The volumes of all subjects were normalized to 1 L during processing. The procrustes aligned mesh was represented by

$$\mathbf{B} = [\bar{\mathbf{x}}_1 \ \bar{\mathbf{y}}_1 \ \bar{\mathbf{z}}_1 \ \bar{\mathbf{x}}_2 \ \bar{\mathbf{y}}_2 \ \bar{\mathbf{z}}_2 \ \cdots \ \bar{\mathbf{x}}_p \ \bar{\mathbf{y}}_p \ \bar{\mathbf{z}}_p] \quad (2.1)$$

where p is the total number of nodes of all the subjects (2550 nodes for our study, for 30 subjects in total), and the over-line represents GPA to the mean. The matrix B was decomposed into modes of shape variation by a PCA. PCA is a statistical procedure that uses an orthogonal transformation to find the principle modes of variation in a sample, through analyzing the eigenvectors and eigenvalues of the covariance matrix of the data matrix B. In this study each mode represents one type of lung and fissure surface shape variation. The first seven principal components accounted for over 90% of the total variation in the training set. The PCA provides a definition of a statistically averaged lung and fissure surface shape, which is the statistical shape model (SSM) that is referred to in the following sections. A second SSM was derived for the training set that did not include the fissure surfaces and so only described the shape of the lung surface.

2.4.3 Initial prediction of lobar location in an individual

The two SSMs were used to predict the fissure locations for subjects that were not part of the training set, using only the definition of the lung surface for the subject as input. A finite element mesh of the lung surface (without fissure information) was generated for a new subject. This lung surface mesh was projected on to the lung surface SSM (with no fissure surfaces). The principal component weight values were calculated from the projection and these weights were used to deform the SSM that contained both lung and fissure surfaces to the subject, to give an initial estimation of fissure locations (Fig 2(c) (d)). This initial prediction of lobar fissures provides a reduced search area for subsequent image analysis and ensures an estimation of complete lobar structures even

if a fissure is incomplete or is difficult to detect in a small region of the image.

2.4.4 Multiscale Hessian-based fissure detection

The location of the SSM predicted fissure planes (Fig 2 (c)(d) were used to guide a Hessian based fissure detection in an individual. Gaussian filters with kernel sizes from 0.5-2.5 mm in 0.5 mm increments were applied to the image set. The responses at each kernel were combined to get a maximum response for each voxel of the image. This multiscale operation guarantees fissures of variable size can be captured by Hessian operations. At each image voxel, the Hessian matrix was constructed as a symmetric matrix. For a fissure structure, which presents as a light plane on a dark background, two large positive second derivatives across the plane and a small second derivative (of either sign) along the plane are expected. This is reflected in the Hessian matrix as two small eigenvalues corresponding to the eigenvectors along the fissure planes and one large eigenvalue perpendicular to the plane. Thus with the relationship of eigenvalues $\lambda_1, \lambda_2, \lambda_3$ defined as $|\lambda_1| \leq |\lambda_2| \leq |\lambda_3|$, λ_3 is expected to be much larger than λ_1 and λ_2 at the fissure. From these characteristics, the fissure probability of each voxel is

$$\text{equation} \quad (2.2)$$

The parameter δ suppresses points whose largest eigenvalue λ_3 is positive, since fissures are locally bright , and is defined as

$$\text{equation} \quad (2.3)$$

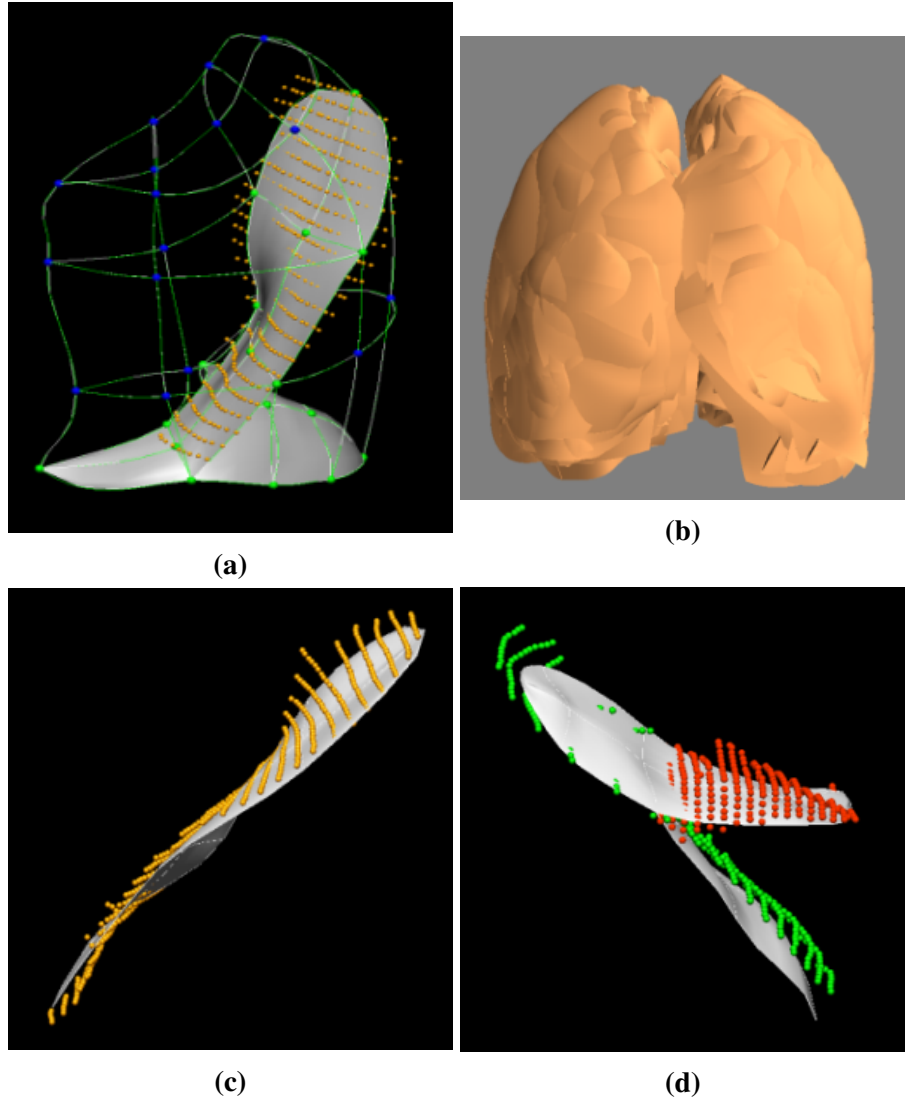


Figure 2.1: SSM initial fissure prediction results. (a) Lung surface fitting and manually-digitized fissure data. (b) Procrustes aligned meshes of 30 subjects. (c) (d) Fissure prediction (white) compared to ground truth fissure points.

S_{plane} detects plane or curve-like structures by searching for locations where λ_3 and λ_2 are significantly different:

$$equation \quad (2.4)$$

S_{wall} suppresses signal of noise and blob-like structures:

$$equation \quad (2.5)$$

p and w are both set to 0.5 as thresholding in this study. S then gives a high response to local sheet-like structures (fissures) and suppresses other pulmonary structures. An example of this filter applied in an individual is shown in Fig 3(a). Blood vessels, which appear as similar structures locally to fissures, are removed from the fissure enhanced result using previous described methods, which removes tube-like structures with $| \lambda_1 | \approx 0$, $| \lambda_1 | \ll | \lambda_2 |$, $| \lambda_2 | \approx | \lambda_3 |$ (Fig 3(b)) [12]. The fissure location predicted by this method allows definition of a search region for the fissure (Fig 3(c)). Candidate points were selected within a fixed distance of the initial fissure approximation: the search distance was set to 20 voxels for left and right oblique fissures and 15 voxels for right horizontal fissure initially. A 2D 4-neighborhood connected component filter and a 3D 6-neighborhood vector-based connected component filter were employed successively to eliminate noise arising from small plane-like structures in this search region (Fig 3(d)). The vector-based connected component filter uses the inner product of the normalized largest eigenvector of the Hessian matrix in adjacent voxels. These largest eigenvectors are perpendicular to the fissure plane, and their inner product provides a criterion for component connection. As the curvature of a fissure is locally low, adjacent fissure voxels should have similar largest eigenvectors and thus large inner product values. The detected points were then divided into a set of small subsections corresponding

to different x, y intervals. For each subsection, the point of the highest fissure probability (the highest S value) was selected as the final candidate fissure point (Fig 3(e)). Then a continuous smooth fissure surface was generated using a B-spline method with a thin-plane spline and extrapolated to the lung boundaries, see Fig 3(f).

2.4.5 Interactive user control interface

As we discussed above, a series of parameter values need to be chosen correctly to ensure a successful lobar segmentation. However, one fixed value of parameter is usually not suitable for all the subjects due to a wide variation of lung tissue and fissure appearances across the population. Therefore, a fast and convenient interactive way to control the segmentation procedure is reasonable and acceptable. Based on an open source Pulmonary Toolkit (PTK, <https://github.com/tomdoel/pulmonarytoolkit>), we developed an improved user-friendly interactive interface to control the segmentation parameters as input. By making use of some built-in objects and visualization system of PTK, we add our lobar segmentation algorithm into the algorithm package and make parameter control buttons available on the interface (Fig 5).

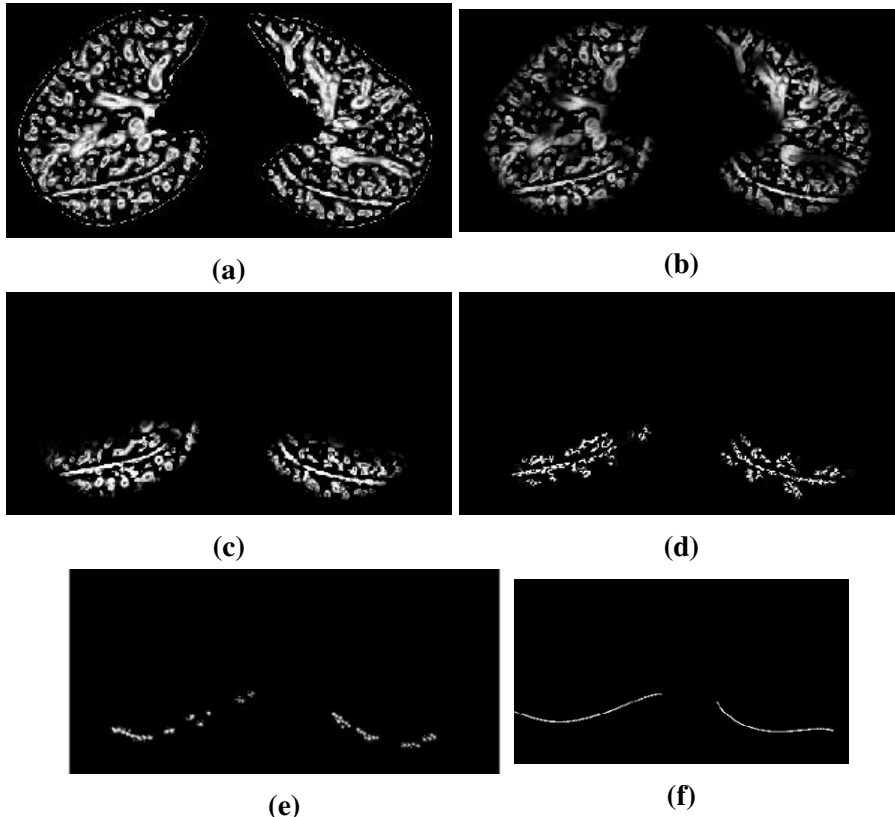


Figure 2.2: Hessian-based multiscale fissure detection results. (a) Hessian-based fissure enhancement. (b) Remove vessel voxels. (c) ROI of fissure locations based on SSM projection. (d) 2D and 3D eigenvector based connected component filter. (e) Fissure candidate points. (f) B-spline curve fissure surface fitting.

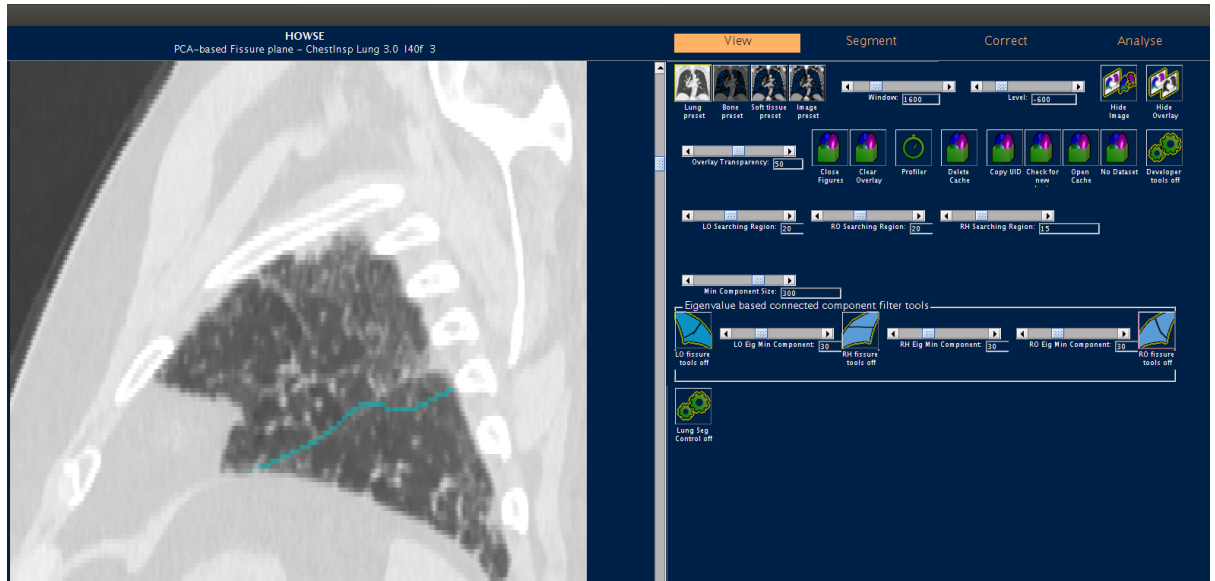


Figure 2.3: User interactive interface.

Search region control

Connected component analysis filter control

Manual correction

2.5 Experiment

2.5.1 Data

The semi-automatic method was tested on two datasets: 1) CT images from five young normal volunteers taken at different lung volumes (end inspiration and end expiration) and with a range of slice thickness (0.5-0.7 mm); 2) CT images from older patients (slice thickness 1.25-3.00 mm) acquired during routine diagnostic inspection for idiopathic pulmonary fibrosis (IPF). Access to clinical data was approved by the Southern Health and Disability Ethics Committee.

2.5.2 Result

The ability of the method to provide an initial estimate of the fissure locations was compared with an interactive watershed transform method [6]. We tested two watered-based segmentation softwares here: 1. Pulmonary Toolkit, <https://github.com/tomdoel/pulmonarytoolkit>; 2. Pulmonary Analysis Software Suite [14]. The two segmentation softwares tested for comparison were unable to segment 7/20 and 9/20 subjects respectively (1/10 and 2/10 normal and 6/10 and 7/10 IPF subjects). In contrast, the model-based method gave an initial estimate for all subjects at all volumes. To quantitatively assess the accuracy of the lobar segmentation method in the normal and IPF subjects, the semi-automatic segmentation was compared with gold-standard manual segmentations. Segmentation accuracy was quantitatively evaluated by computing the mean difference and percentage of fissure points ± 3 mm between the gold-standard and semi-automatic method (Fig 4). The 3 mm criterion approximates the thickness of CT images routinely used clinically [13]. For normal subjects, the average mean differences (and accuracies) were 2.06 mm (78%), 4.06 mm (62%), and 2.85 mm (72%), for left oblique, right horizontal and right oblique fissures, respectively. For IPF subjects, the average mean differences (and accuracies) were 3.41 mm (66%), 5.79 mm (56%), and 5.01 mm (60%), for left oblique, right horizontal and right oblique fissures, respectively.

Fig 5 shows the spatial distribution of error for three representative subjects. Error was highest in regions close to the hilum (where the anatomical structures are complex, and/or the fissure is often incomplete), and where the right fissures meet.

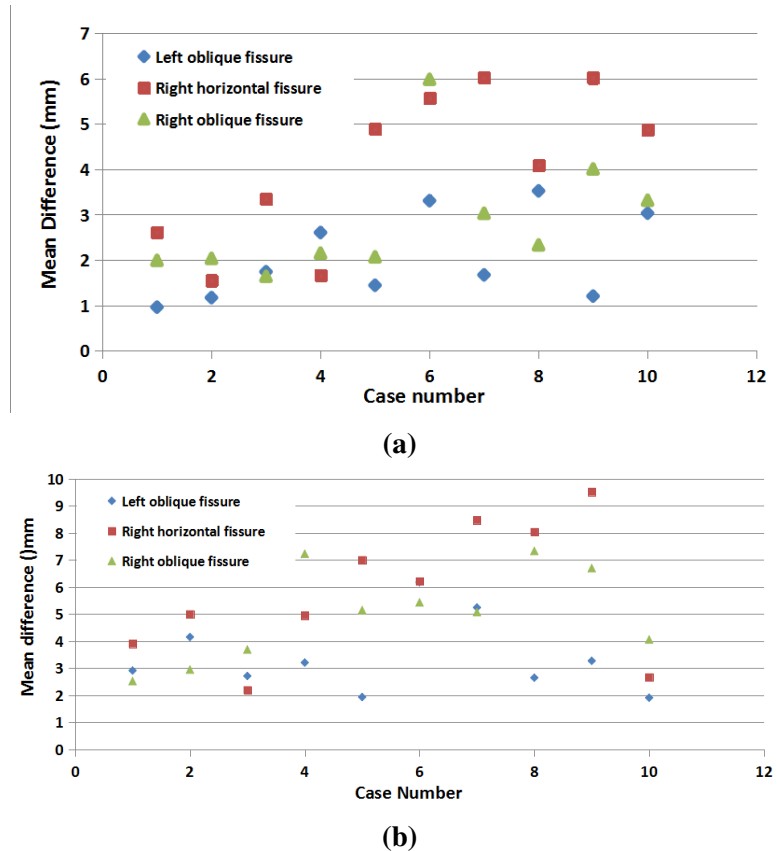


Figure 2.4: Quantitative evaluation results of the segmentation accuracy. (a) Mean difference for normal young subjects. (b) Mean difference for IPF subjects.

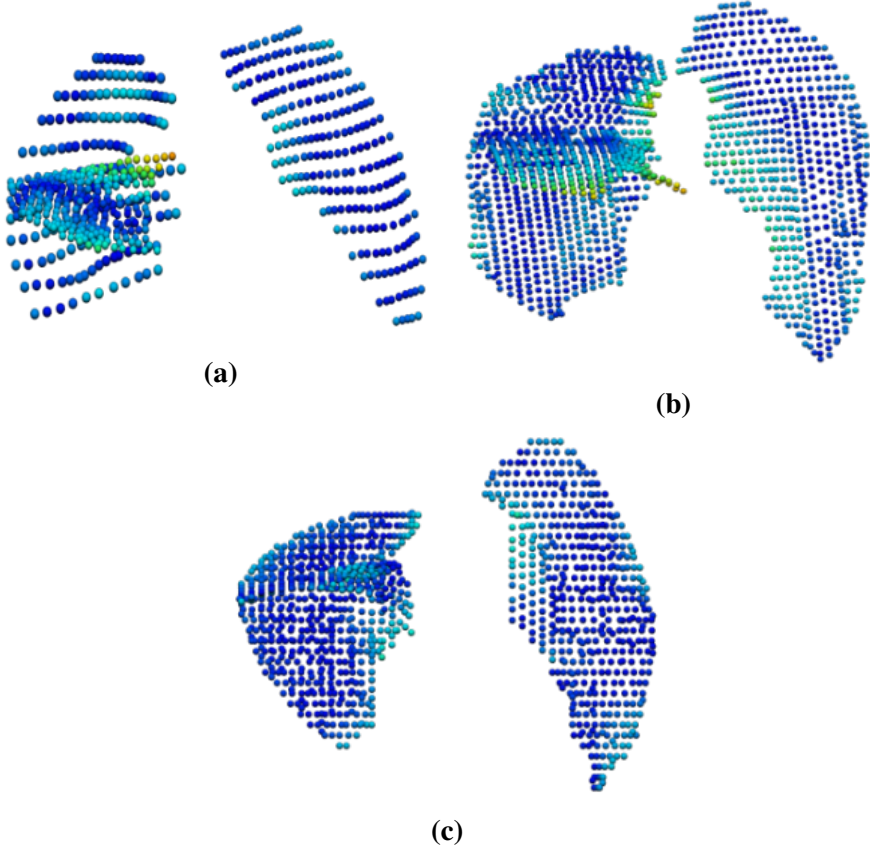


Figure 2.5: The spatial distribution of error between the gold-standard and semi-automatic methods for three representative subjects, highlighting localized regions of low accuracy.

2.6 Discussion

In this paper, we presented a pulmonary lobar segmentation method. Results show that the method can perform well to detect the location of the fissures over most of the fissure surfaces on CT images from normal subjects, and provides a relatively accurate result for most of the IPF (abnormal) subjects. Due to lower imaging resolution and tissue abnormalities, the accuracy of the method was lower for the IPF subjects. The method performed better on the left oblique fissure than the other two fissures, because the left lung has a simpler anatomic structure with only one fissure. In contrast, misdetection

happens more often in the area of right lung where the two fissures come into contact. This is illustrated in Fig 5, which shows the error distribution over the three fissures for three subjects. It can also be seen that the method results in higher error in the lung boundary area, since the fissures here are commonly incomplete, thus few fissure candidate points can be detected accurately. Compared to the current published anatomical structure-based methods, the model-based method can predict an initial fissure location without requiring an accurate preliminary analysis of other anatomical features. For example, traditional anatomical knowledge-based methods such as the watershed-based lobar segmentation need to label the airway trees to the five main lobar bronchi to get an initial fissure approximation. However, due to the complex radiological appearance of pathological lungs, it is usually difficult to get a reliable airway and vessel tree segmentation. This was the case in our comparison of the model-based estimation of fissure location with a watershed-based method; the latter failed for nearly half of the subjects.

Chapter 3

Quantitative analysis of idiopathic pulmonary fibrosis abnormality from CT scans

The following chapter outline the study of quantitative analysis of idiopathic pulmonary fibrosis abnormality from CT scans. This chapter is divided into (1) challenges of IPF diagnosis, (2) advantages of quantitative analysis using HRCT, (3) review of current published methods of quantitative analysis of IPF, (4) method of IPF quantitative analysis (5) experiment and (6) discussion.

3.1 Challenges of IPF diagnosis

IPF progression is variable and unpredictable. Some studies indicate that 15% of patients with IPF experience a rapid worsening of symptoms, insufficiency of pulmonary function and over 80% of these rapid progressive patients die of respiratory failure

within 6 months. Most IPF patients deteriorate relatively slowly, and their pulmonary function usually decreases gradually over the months to years after the first clinical symptoms [1]. However, there are currently no reliable biomarkers that indicate the likely progression of IPF disease [4]. Accurate assessment and diagnosis of IPF disease is a challenging task due to significant individual physiological differences and variable disease progression [4]. The American Thoracic Society (ATS)/ European Respiratory Society (ERS) provides a diagnostic criteria and schema for adult patients with IPF [5], and this criteria strongly recommends a multidisciplinary discussion between pulmonologists, radiologists and pathologists for an accurate diagnosis [5]. However, a successful classification scheme that allows recognition of disease identically across radiology, pulmonary and pathology disciplines remains difficult.

3.2 Advantages of quantitative analysis using HRCT

Recent development in radiological imaging techniques offers exciting opportunities to provide radiological patient-specific biomarkers as important indicators of specific phenotypes [4,6-7]. High-resolution computed tomography (HRCT) has played an essential role in evaluating lung disease through recognizing visual patterns and features of disease regions such as ground-glass opacities, reticular patterns and honeycombing. HRCT is a useful diagnostic tool for the characterization and classification of IPF and differentiate between IPF and other pathologies such as usual interstitial pneumonitis (UIP), nonspecific interstitial pneumonitis (NSIP) and other interstitial lung disease (ILD) which has a similar clinical phenotype. Based on the criteria of IPF set by members of ATS / ERS [5], the diagnosis of IPF usually associates with the presence of a usual interstitial pneumonia (UIP) pattern on HRCT. Honeycombing is characterized

by clustered cystic air spaces, cysts of comparable diameters, and cyst diameters typically $>10\text{mm}$ surrounded by well-defined walls. Reticular opacities, often associated with traction bronchiectasis. Ground-glass opacities are common, but usually less extensive than the reticulation. The distribution of UIP on HRCT is characteristically basal and peripheral (subplerual), though often patchy. Currently, the detection of disease change over time and how these changes can predict disease progression is still a developing problem. Manual classification and subjective evaluation are usually complicated and not accurate enough. Image-based quantitative analysis is therefore strongly needed for developing a robust and consistent IPF assessment system [6-8].

3.3 Review of current published methods of quantitative analysis of IPF

In the past few years, there has been considerable effort to provide quantitative analysis on CT scans of lung parenchymal abnormalities. Renuka et al [9-10] was an early group to present a computer aided diagnosis (CAD) method to quantify lung tissues based upon HRCT. An adaptive multiple feature method (AMFM) which combined statistical texture measures and a fractal measure was developed to assess CT features for classifying a tissue pattern. Alan et al [11-12] used mean lung attenuation (MLA), skewness (asymmetry) and kurtosis (peakedness) as quantitative CT indexes and furtherly used univariate and multiple correlation and regression statistical analyses to determine relationships between histogram features and results of PFTs. Hyun et al [13-15] published a series of papers presenting a texture-based CAD scoring system to assess quantitative lung fibrosis (QLF) as a measurement of lung disease severity and as

a surrogate imaging marker. Brian et al [16-18] developed a software for analysis of thoracic HRCT through classifying CT imaging into texture patterns such as honeycomb, reticular and ground-glass, thus providing a reproducible way to quantify and characterize lung parenchymal disease. However, the current published methods mainly focus on the global analysis of each CT pattern or texture-based index as a whole lung (such as the percentile analysis or the correlation between indexes), but seldom characterize the spatial distribution of each diseased region or the change extent of these abnormalities.

3.4 Method of IPF quantitative analysis

We aim to analyze and characterize IPF tissue abnormalities over time using quantitative methods. HRCT imaging is classified by pattern using a validated image analysis process [16-18]. The data is mapped to a statistical shape model allowing a quantitative approach to analyze tissue density, tissue volume, the spatial distribution of abnormalities, and regional changes in tissue over time. The tissue density, tissue volume and the location of abnormality are all important indexes for representing a quantitative statistical progression of IPF disease. We hypothesize that this quantitative analysis would provide consistent potential tissue-level markers to help with the further modeling of mechanical ventilation/perfusion mismatch and impaired gas exchange.

3.4.1 Pulmonary parenchymal classification

Tissue regions were classified using CALIPER (Computer-Aided Lung Informatics for Pathology Evaluation and Ratings) software. CALIPER is a computational image analysis platform developed by the Biomedical Imaging Resource Laboratory at the Mayo Clinic Rochester (Rochester, MN, USA) for the characterization and classification of

lung parenchymal findings on high-resolution computed tomography (HRCT) [16-18]. CALPER isolates regions of the lung parenchyma by extracting central airways and vascular structures and classifies every parenchymal voxel into the following characteristic CT patterns: normal (N), reticular (R), honeycomb (HC), ground-glass (GG), mild low attenuation areas (LAA), moderate LAA and severe LAA. In addition, emphysema areas were extracted through detecting the voxels whose Hounsfield Unit is under -950.

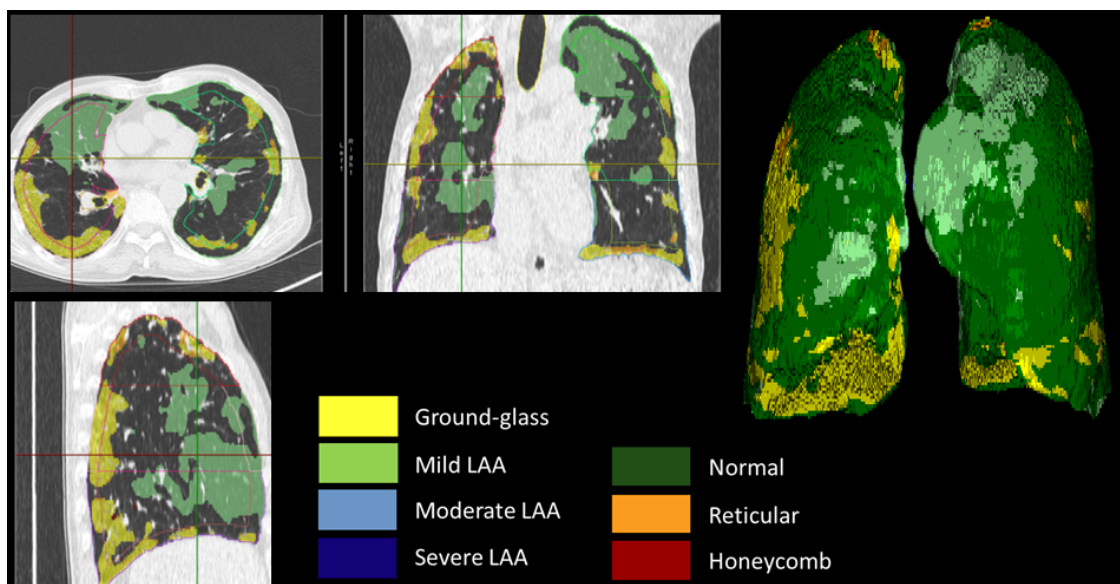


Figure 3.1: Color labelled classification result of case 7 on IPF HRCT by CALIPER. (a) Transverse plane. (b) Coronal plane. (c) Sagittal plane. (d) 3D color labelled lung.

The volumetric classification of pulmonary parenchyma by CALPER is based on histogram signature mapping techniques. Multiple 15*15*15-pixel volumes of interest (VOI), neighborhood of each of the parenchymal voxel were selected through independent analysis by four subspecialty thoracic radiologists from CT scans. The local histograms computed from these VOIs were compared against the histogram of 34 exemplars identified in the training phase to determine if visual appearance of 70% or more of the given VOI spanning 15*15*15 voxels was normal, contains emphysema or

belonged to one of the above characteristic IPF parenchymal CT patterns. The exemplars were selected by all four radiologists with agreement on the class of each kind of abnormalities Cramer Von Mises (CVM) dissimilarity measure was used in the comparison and the fundamental type of the exemplar with the least CVM and automatic cluster affinity techniques distance was assigned as the parenchymal class of the underlying voxel. Fig.1 shows a representative dataset with axial, coronal and sagittal sections of a CT lung volume where every voxel of the parenchyma is characterized and color coded into one of the parenchymal patterns (N, R, H, G, and mild, moderate and severe LAA).

3.4.2 Normalization of classified data

Lung surface data was extracted from CALIPER output and fissure surfaces were defined manually using the open-source visualization software CMGUI (<https://www.cmiss.org/cogui>) by an expert user. A bi-cubic Hermite finite element surface mesh was fitted to the shape of the lung and its fissures via a least squares fit (<https://www.cmiss.org>). The average root mean square (RMS) error of this fitting method was 0.5-0.7 mm for each subject. The mesh structure is consistent for each subject to allow landmark points to be defined. The left lung mesh consists of 35 nodes and 44 elements, while the right lung mesh has 50 nodes and 62 elements. Each node has 12 degrees of freedom (DoF) which store the global coordinates and first and second nodal derivatives. Each node is either an anatomical landmark (the left/right lung apex, the base vertex, the shape corner and the center point of the middle line of fissure) or a pseudo-landmark (a fixed proportion of the arc-length between two anatomical landmarks). There is lung shape variation between different subjects and often between clinical images obtained at different times, as well as variation in the extent to which a patient inhales for imaging, even with careful train-

ing. Thus, classified volumetric lung data was then mapped to a statistical shape model (SSM) of the normal older human lung to provide a consistent mapping of tissue abnormalities between and within individuals to a same lung shape. The SSM is an average mesh of the lung lobe which derived from a set of training segmented lung and fissure surface locations. It has the same geometric mesh connectivity as the above introduced lobe mesh. The training set consisted of data from 30 healthy normal subjects (15 males and 15 females) that was retrospectively selected from the Human Lung Atlas (HLA) database (image acquisition for this previous study was approved by the local ethics and radiation safety committees, and subjects gave informed consent). To construct the SSM, the location and derivatives at each node (landmark or pseudo-landmark) in the finite element mesh was used in a principal component analysis (PCA) conducted on the training set [19-21]. The SSM provides a definition of a statistically averaged lung and fissure surface shape, which is the statistical shape model (SSM) that is referred to in the following sections. In order to map the individual classified data to the SSM mesh, all of the classified data should be completely enclosed inside its fitted lobe surface mesh. The position of each point within the finite element mesh is defined locally in each element of the mesh by ξ_i , for $i=1,..,3$ with $0 < \xi_i < 1$. The local coordinate ξ_i was then used to calculate the global coordinates of the mapped data points using the following equation:

$$equation \quad (3.1)$$

where \mathbf{u}_n is a vector of N element nodal parameters of the SSM lobe mesh associated with the interpolation functions Ψ_n . The mapped classified data is shown in Fig 2(a). In order to make the data points distribute uniformly throughout each lung, the gap sin of the mapped data caused by the deformation (shown in Fig 2(b)) were filled to match

their closest neighbor point among the classified data, so that it could be easier for the further volume and density quantitative analysis. The filled data of case 6 is shown in Fig 2(c).

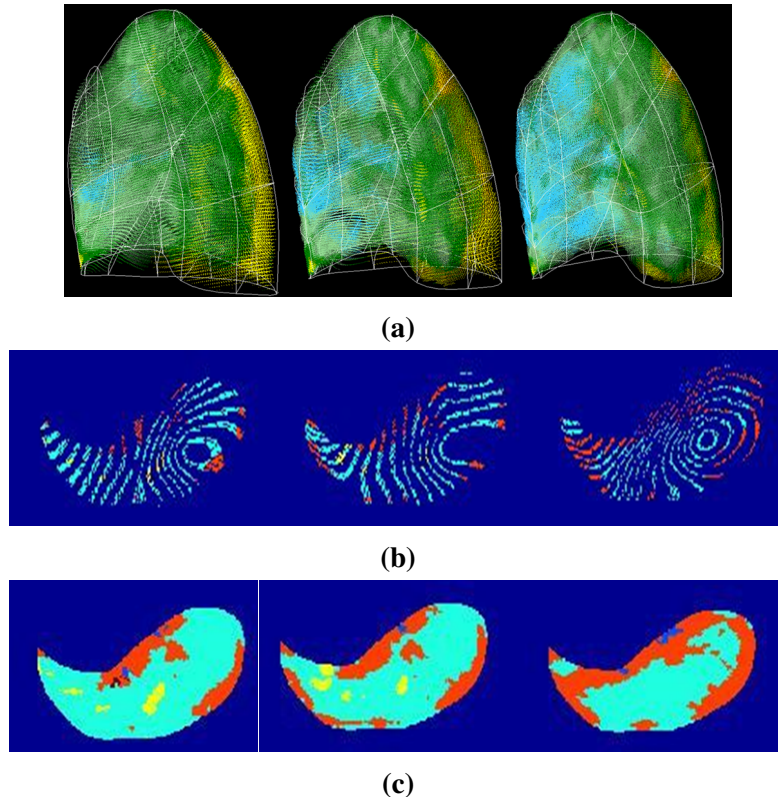


Figure 3.2: Classified data normalization result of three time points for case 6. (a) SSM based mapping result of the three time points. (b) Ununiformed gap slice after mapping. (c) Gap filled slice of the three time points. The three time points are shown in the same position and same slice number.

3.4.3 Quantitative analysis of imaging data

Density analysis

The average density value of each classified region was calculated. The pixel intensity values in a typical CT image correspond linearly to the actual density of the imaged

tissue. Density is measured in Hounsfield units (HU), with our segmentation software calibrated to values of approximately -1000 for air density, zero for water density, and over 40 for blood, bone, and other non-parenchymal tissue. The average density of each CT pattern was calculated.

Volume analysis

The volume of the lung comprising each classified, connected region n was calculated using the following equation:

$$\text{equation} \quad (3.2)$$

where N is the number of voxels of this region, R_x , R_y are the x, y resolution of the CT scan, and R_z is the thickness of the CT scan.

Spatial distribution analysis

In order to quantitatively analyze the spatial distribution of IPF disease, the location distribution of honeycomb, reticular, emphysema and ground-glass CT patterns which represent UIP disease patterns on HRCT were measured focusing on the three following aspects: Basal-to apical: In the direction from base to apex, the volume percentage of each disease region was averaged in 5% percent lung height (along the dorsoventral axis). Also, the volume percentage of each disease region for each lobe was calculated to provide a lobar distribution of disease. Subplerual to internal: The percentage from the center of the lung to the boundary of the lung was used as a credible measurement to analyze the peripheral performance of disease. The center location of each connected cluster of disease pattern was firstly calculated. As the point position shown in Fig.3, the subplerual to internal percentage of each connected cluster of disease region was

calculated by:

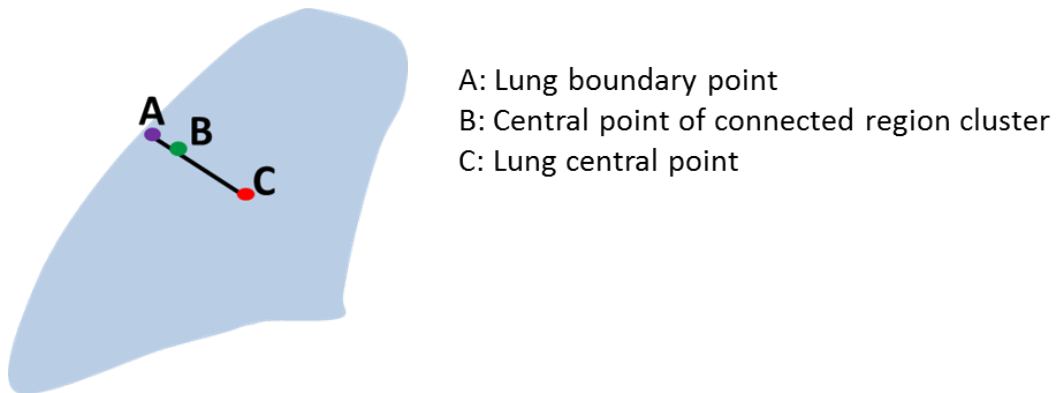


Figure 3.3: Subpleural-to-internal percentage calculation diagram.

Diseased CT pattern change over time

Median survival among persons with IPF is believed to be from 3 to 5 years. However, individual progressive performance is variable and how the characteristic CT pattern change in this period of time (e.g. whether a disease region change to other CT patterns or stay the same over time) still remains elusive. As the lung has been normalized into the same standard shape, the mapped lung of each time point should have the same number of voxels. For each voxel, the CT pattern of each time point is extracted, so that it is available for us to detect the change for each area of lung over time.

Shape analysis

Compare the shape of IPF subjects to normal population.

3.5 Experiment

3.5.1 Imaging and clinical data

The clinical data used in this study comprised HRCT images obtained from 8 patients diagnosed with IPF at Auckland City Hospital, Auckland, New Zealand. Data acquisition was approved by the Southern Health and Disability Ethics Committee (ETHICS APPROVAL NUMBER). Clinical HRCT images (slice thickness 1.25-3.00 mm) were acquired during routine diagnostic inspection and/or monitoring for IPF disease. Four of the subjects had more than one serial CT scans within 5-20 month interval, representing different time point.

Table 3.1: Demographic data.

| Description | |
|---------------------|--------------|
| Age years | 43-82 |
| Females/Males | 3/5 |
| Slice thickness | 1.23-3.00 mm |
| Scan month interval | 5-20 month |
| Slice resolution | 512 × 512 |
| Number of slice | 65-160 |

3.5.2 Results

Density analysis

The density analysis result is shown in Fig.4 It can be seen from the result that the average density of each region almost remains consistent over time, and for one region, the tissue density usually slightly fluctuates within a specific range. Meanwhile, the value interval of different CT pattern has little intersection with each other. The ground-glass region has the highest average tissue density and emphysema has the lowest average

tissue density. That means it is possible to regard tissue density as a measurement index to distinguish the disease region from other lung parenchyma.

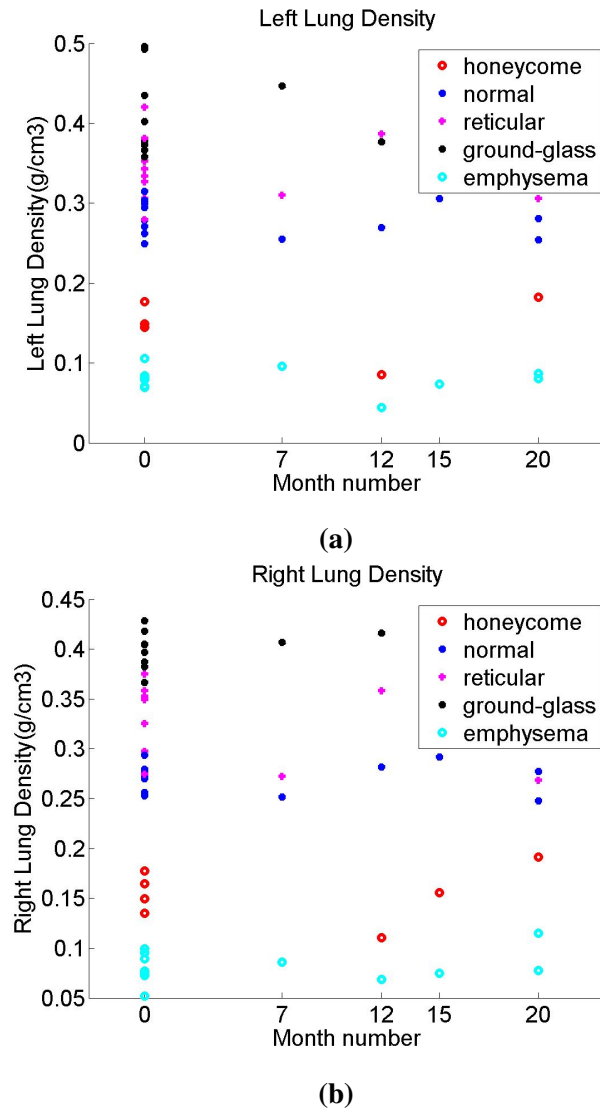


Figure 3.4: Average density (g/cm^3) of each CT pattern for IPF left and right lung. Each point represents the average density of one CT pattern for each lung. X axis shows the month interval of scan time for each patient, and 0 represents the first scan for this patient. (a) Left lung. (b) Right lung.

Volume analysis

Fig.5. shows the volume changes of different regions over time for case 6. Table 1 shows the whole volume of each lung for each time point. It can be seen that the lung volume of IPF patient keeps decreasing as a whole over time.

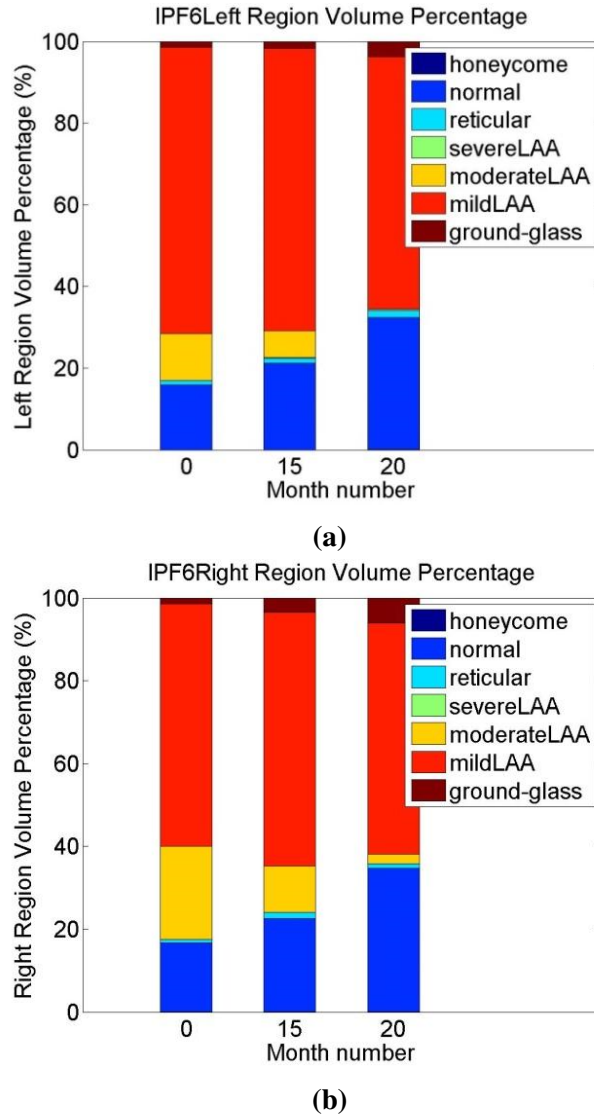


Figure 3.5: Volume percentage change of each CT pattern over time for case 6. (a) Left lung. (b) Right lung..

Table 3.2: Whole volume of left and right for each time point($1.0e_5 * mm_3$).

| Sub No. | Time point | Date Left | Lung Right | Lung |
|---------|-------------|------------|------------|--------|
| IPF5 | Time pint1 | 02/11/2013 | 4.3124 | 3.7212 |
| | Time point2 | 12/11/2014 | 3.9457 | 3.2861 |
| IPF6 | Time point1 | 15/10/2012 | 6.0889 | 8.9697 |
| | Time point2 | 30/01/2014 | 5.3770 | 7.6340 |
| | Time point3 | 18/06/2014 | 5.1604 | 7.7413 |
| IPF9 | Time point1 | 24/12/2013 | 3.3798 | 3.7271 |
| | Time point2 | 01/07/2014 | 3.0507 | 3.5815 |
| | Time point3 | 12/08/2015 | 3.0814 | 3.8328 |

Spatial distribution analysis

1 Basal-to apical analysis

Fig.7. shows the percentage distribution against lung height (dorsoventral axis) of four characteristic CT patterns: ground-glass, reticular, honeycomb and emphysema for left and right lung. It can be seen from the result that ground-glass region mainly locates in the basal part of lung. The percentage of ground-glass decreases gradually with the increasing of the lung height. In contrast, the percentage of emphysema roughly keeps a rising trend along with the increasing of lung height. The distribution of reticular region mainly focuses on the basal area and apex area. This kind of disease CT pattern seldom appears in the middle part of lung. The distribution of honeycomb seems not to have a regular distribution against lung height.

2 Lobar distribution

Fig.8 shows the percentage of four characteristic CT patterns: ground-glass, reticular, honeycomb and emphysema for the five lobes (left upper, left lower, right upper, right middle, right lower). For ground-glass and honeycomb patterns, it can be seen from the figure that the disease regions mostly locate in the lower lobe of each lung. For reticular pattern, the percentage of middle lobe is significant lower than the percentage

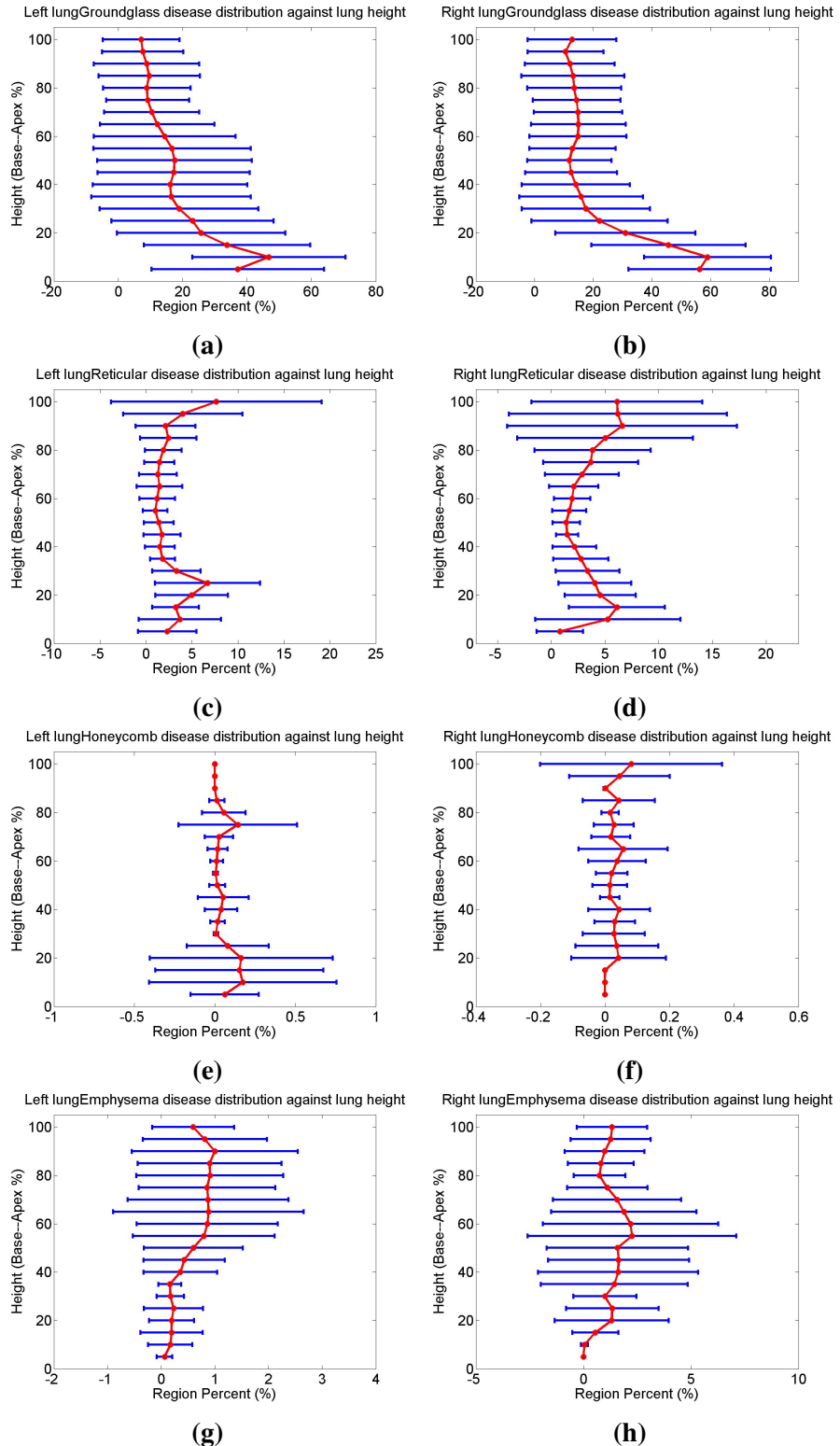


Figure 3.6: Percentage of each disease CT pattern against lung height (dorsoventral axis) for IPF left and right lung. The region percentage was calculated averagely within 5% of the lung height from the base to the apex. Red line represents the average value of this position across all patient, and blue line shows the standard deviation. (a) (b) is the ground-glass pattern distribution against lung height for left and right lung. (c) (d) is the reticular pattern distribution against lung height for left and right lung. (e) (f) is the honeycomb pattern distribution against lung height for left and right lung. (g) (h) is the emphysema pattern distribution against lung height for left and right lung.

of other lobes, which probably means reticular pattern hardly locates in the middle part of lung. As for emphysema lesions, it commonly distributes in the upper lobes and with the increasing of time, it may also appear in the middle lobe.

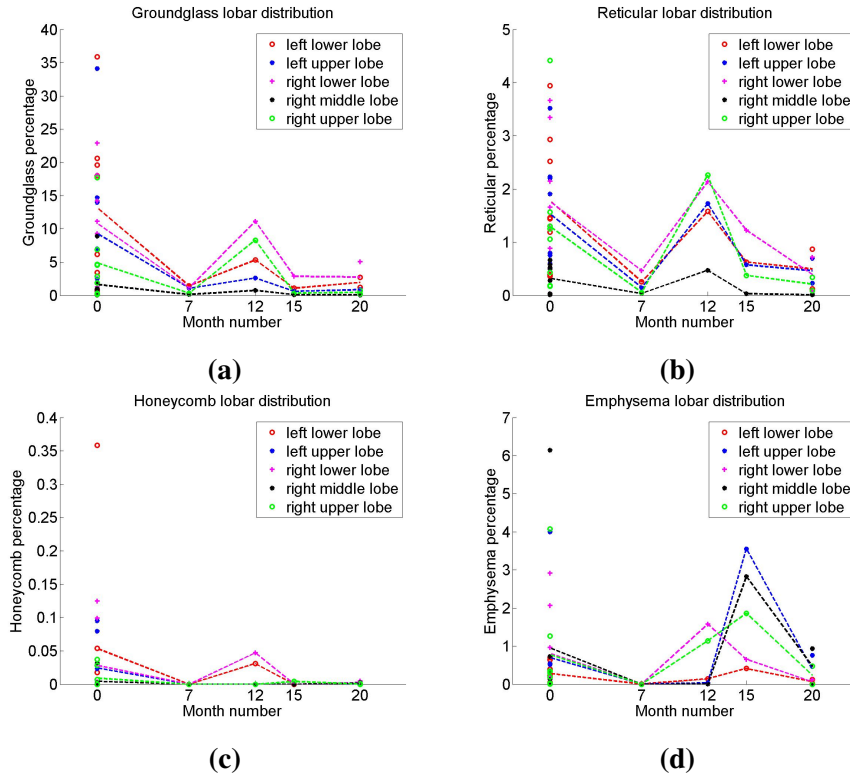


Figure 3.7: Lobar distribution of CT patterns. X axis shows the month interval of scan time for each patient, and 0 represents the first scan for this patient. Each point represents the percentage of one CT pattern for one lobe. The dotted line represents the average value for each time point. (a) Ground-glass lobar distribution. (b) Reticular lobar distribution. (c) Honeycomb lobar distribution. (d) Emphysema lobar distribution.

3 Subpleural-to-internal analysis

Fig.9 shows the subpleural-to-internal percentage of each connected cluster of the three CT patterns: ground-glass, reticular, honeycomb and emphysema. Most of the disease clusters are peripheral performance. For both left and right lungs, the subpleural-to-internal percentage of most disease clusters are under 20%. That means the IPF disease

are usually peripheral performance and mainly distributes surrounding the surface of the lung.

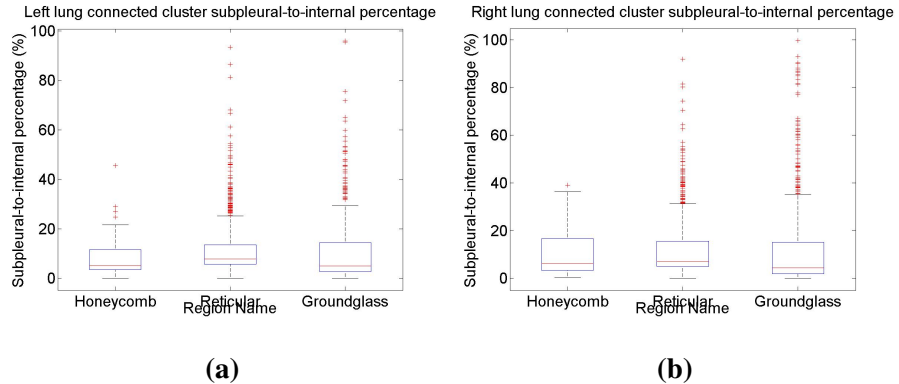


Figure 3.8: Subpleural-to-internal percentage of connected CT pattern cluster for IPF left and right lung. (a) Left lung. (b) Right lung.

CT pattern change

Table 2 shows how the two characteristic disease CT patterns (ground-glass and reticular) change over time. It describes the percentage of each CT pattern which changes from ground-glass or reticular pattern of the previous time point. For ground-glass region of both left and right lungs, over 50% of this region still stays the same pattern over time, whereas there are also some area of ground-glass change to normal or reticular pattern as time goes by. The pattern changes is more significant for reticular region, although quite a number of reticular area didnt change over this period of time, a large proportion of it change to ground-glass, especially for right lung, and there is also about 10%-30% of reticular becoming normal during this time. In general, it seems that the IPF disease area is changing all the time. One kind of disease pattern may change to other pattern, and some parts of disease area may change to a normal one.

Table 3.3: CT pattern change over time of left lung for case 6 (%).

| Time1 | Time2 | Ground-glass | Mild-LAA | Moderate-LAA | Normal | Reticular | Honeycomb | Severe-LAA |
|-------|-------|---------------------------|---------------------|--------------|---------------|----------------|---------------|------------|
| Time1 | Time2 | Ground-glass Reticular | 53.65 29.76 | 0.36 3.01 | 0.37.31 0 | 8.65 28.41 | 0 38.82 | 0.03 0 |
| | Time3 | Ground-glass Reticular | 71.61 39.94 0.83 | 0.13 0 | 0.03 16.59 | 15.41 42.56 | 12.82 0.07 | 0 0 |
| Time1 | Time3 | Ground-glass Reticular | 70.01 37.97 | 0.83 4.73 | 0 0 | 20.80 15.49 | 8.35 41.81 | 0.01 0 |
| | | | | | | | | |

The time interval from time point 1 to time point 2 is 15 months, the time interval from time point 1 to time point 2 is 5 months, the time interval from time point 1 to time point 3 is 20 months.

Table 3.4: CT pattern change over time of left lung for case 6 (%).

| | | Ground-glass | Mild-LAA | Moderate-LAA | Normal | Reticular | Honeycomb | Severe-LAA |
|-------|--------------|--------------|----------|--------------|--------|-----------|-----------|------------|
| Time1 | Ground-glass | 61.76 | 4.15 | 0.92 | 7.14 | 25.92 | 0 | 0.11 |
| | Reticular | 47.61 | 6.88 | 0.01 | 11.10 | 34.37 | 0 | 0.03 |
| Time2 | Ground-glass | 78.16 | 0.08 | 0.01 | 18.51 | 3.23 | 0 | 0.05 |
| | Reticular | 55.74 | 0.44 | 0 | 31.46 | 12.35 | 0.01 | 0 |
| Time1 | Ground-glass | 79.98 | 1.82 | 1.63 | 12.82 | 3.45 | 0 | 0.30 |
| | Reticular | 65.80 | 3.28 | 0.02 | 19.40 | 11.33 | 0 | 0.16 |

The time interval from time point 1 to time point 2 is 15 months, the time interval from time point 1 to time point 2 is 5 months, the time interval from time point 1 to time point 3 is 20 months.

Shape analysis

1 Shape difference for each mode The results show that there is no significant shape

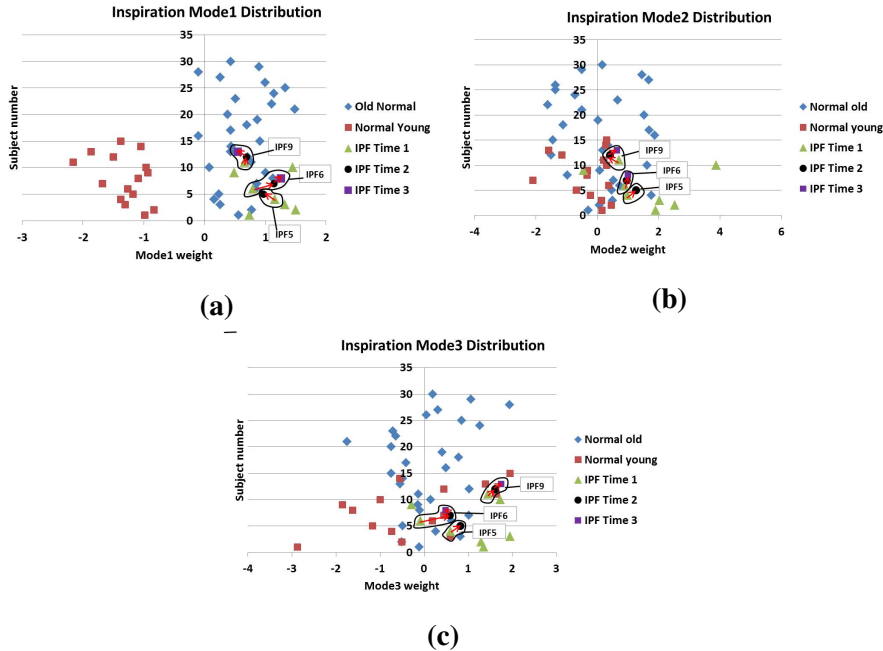


Figure 3.9: Shape differences between IPF subjects and normal subjects for the first three mode (a) Mode 1. (b) Mode 2. (c) Mode 3. Arrow tracks the mode weight changes over time.

difference between IPF subjects and normal ones.

2 Mahalonobis distance

3.6 Discussion

IPF is a progressive lung disease that has significant variable expression between different patients. Our SSM based quantitative method normalized a set of lungs of different shapes into a standard shape model, thus providing a convenient way to make a reliable

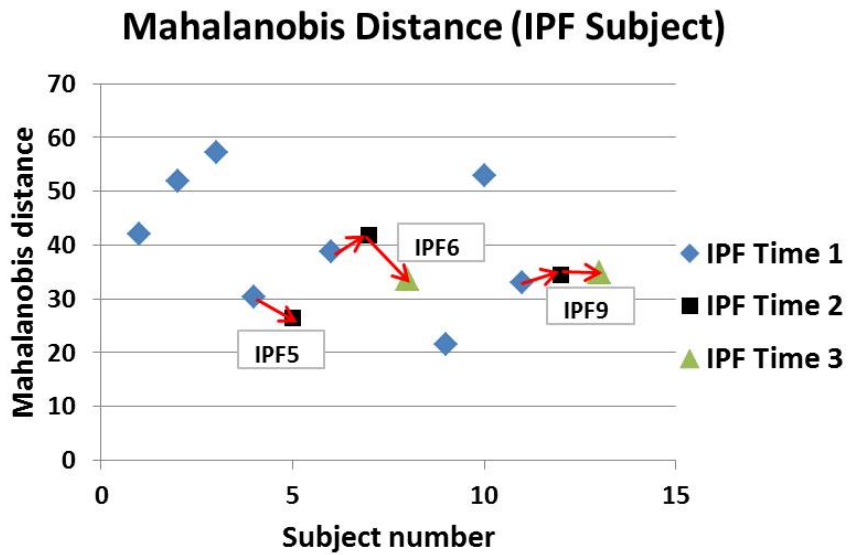


Figure 3.10: Mahalonobis distance of IPF subjects

comparison between different patients or within one patient of different time points. This method makes it possible to capture the disease variation across a population and represent the difference using objective values. Meanwhile, the progression of disease over time can be described, and this will be quite helpful to predict the tendency of disease in clinical practice. The tissue density, disease volume and spatial distribution are all important indices to characterize and analyze the disease. Through quantifying these features instead of qualitative evaluation, subjective errors could be avoided to offer a more consistent assessment. Individualized treatment strategies are urgently needed in clinical applications and are the ultimate goal of modern pulmonary medicine. Quantitative analysis on HRCT images has the potential to build a reliable relationship between imaging tissue-level biomarkers and clinical endpoints, and further could be able to help with medicine development or IPF disease research. But how to translate imaging biomarkers into functional biomarkers for pulmonary function tests (PFTs) and clinical diagnosis is still a challenging work. To test whether these markers are func-

tionally significant, a model based analysis of lung function need to be developed. For IPF patient, ventilation/perfusion mismatch and impaired gas exchange is a frequent occurrence. These imaging biomarkers such as the distribution of disease or the density of disease provide physiological parameters for conducting modeling of IPF lung functions. And the model based analysis will also analyze which quantitative index and which kind of disease is the key factor for the pulmonary function decline of IPF lung. On the other hand, combined IPF and emphysema (CPFE) has been mentioned and defined in the past ten years. Some researchers suggest that CPFE should be regarded as a distinct clinical entity other than emphysema or IPF alone, since it has a characteristic pulmonary function feature different from pure emphysema or IPF. It is commonly believed that CPFE is strongly associated with heavy smokers, severe dyspnea on exertion and impaired gas exchange, and emphysema usually happens in the upper lobe whereas IPF disease tends to appear in the lower lobe which has been proved in our analysis, but whether the presence of the two diseases developing in parallel is still unknown [22-24]. Our image based analysis provides quantitative indices for a further pulmonary functional simulation, which could help understand the relationship between the two diseases and the impact of emphysema on IPF. In addition, it is widely acknowledged that there should be some typical symptoms occurring averagely 1-2 years before a clinical diagnosis with IPF, and even some radiographic evidence of IPF may be found before symptoms occur [1,5]. This subclinical period of disease is very important for an early diagnosis of IPF disease. Our SSM based quantitative method make it available to compare IPF diseased lung to an average old normal lung. Through combining the comparison with a successive disease progressive research together, we could probably get a whole prediction of IPF lung decline from normal state to severe injured state. It can help clinician to recognize abnormalities in a normal lung at subclinical stage, and

this is also the further goal of our research.

Chapter 4

Functional model based analysis of IPF

The model based analysis chapter...

4.1 Functional model introduction

4.2 Functional model analysis

...

Chapter 5

Conclusion

The conclusion chapter...

5.1 Summary

5.2 Limitations

5.3 Future directions

List of References

- Carloni, A., Poletti, V., Fermo, L., Bellomo, N., and Chilosi, M. (2013). Heterogeneous distribution of mechanical stress in human lung: a mathematical approach to evaluate abnormal remodeling in ipf. *Journal of theoretical biology*, 332:136–140. [Cited on page 1.]
- Selman, M. and Pardo, A. (2014). Revealing the pathogenic and aging-related mechanisms of the enigmatic idiopathic pulmonary fibrosis. an integral model. *American journal of respiratory and critical care medicine*, 189(10):1161–1172. [Cited on page 1.]